Original Research Article

Investigation of Mg-doped SnO_2 Nanoparticles as an Efficient Photocatalyst for the Degradation of Crystal Violet Dye

ABSTRACT

This study is an attempt to investigate the photocatalytic performance of magnesium (Mg) doped SnO_2 nanoparticles (NPs) for the degradation of Crystal Violet (CV) dye under sunlight irradiation. Mg doped SnO_2 NPs with varying concentrations of Mg were synthesized through coprecipitation method. The synthesized NPs were characterized using X-ray diffraction (XRD), UV-Vis spectroscopy and Fourier transform infrared (FTIR) spectroscopy to confirm their structural and optical properties. The photocatalytic efficiency of Mg-doped SnO_2 NPs was evaluated by examining the degradation rate of CV dye. The results demonstrated that Mg doping significantly improved the photocatalytic activity of SnO_2 NPs, with a 15wt% Mg doping concentration leading to the highest degradation rate of CV dye. The enhanced photocatalytic performance is attributed to the increased charge carrier separation due to Mg doping. This study highlights the potential of Mg-doped SnO_2 NPs as effective photocatalysts for the degradation of organic pollutants, offering a promising approach for wastewater treatment applications.

Keywords: *Tin oxide (SnO_2), Crystal violet dye, Mg-doped SnO_2 nanoparticles, Doping*

1. INTRODUCTION

The discharge of waste from textiles, paper and dye industries, extensive usage and improper disposal of pesticides and fertilizers in agriculture practices have resulted in a significant rise in various organic contaminants in natural water ecosystems. Many of these organic pollutants are non-biodegradable and through anaerobic degradation they can generate carcinogenic intermediates. The textile industry consumes synthetic dyes more than 10,000 tons annually, which accounts for a fraction of 7×10^7 tons of synthetic dyes produced worldwide each year (Al-Tohamy et al., 2022). The release of these synthetic dyes into the environment causes adverse effects on human health and damages aquatic life and ecosystems (Kant, 2012). Dyes employed across various industries are categorized into cationic, anionic, and non-ionic groups based on their ionic charge. Among these dye categories, cationic dyes are considered to pose a higher level of toxicity when compared to their counterparts (Foroutan et al., 2022). Crystal violet (CV), alternatively referred to as gentian violet, methyl violet 10B, or hexamethyl pararosaniline chloride, is a cationic dye with molecular formula $C_{25}H_{30}N_3Cl$. Fig. 1. illustrates the chemical structure of the CV dye. CV dye finds widespread application in the production of printing inks, paints, and dyes for their subsequent utilization in the textile industry. Beyond serving as a biological stain and playing a central role in Gram's stain, CV dye is also frequently employed for the treatment of bacterial infection, and skin ailments in both humans and animals. Furthermore, it serves as an antifungal, antibacterial and antiparasitic component in poultry feed (Patel et al., 2021) (Blanco-Flores et al., 2014). Nevertheless, extended exposure to these chemicals has been associated with certain health problems, including jaundice, mild eye discomfort, and mutagenic effects. The significant amount of these chemicals when ingested through the skin can be highly toxic to mammalian cells and can induce skin irritation and digestive track irritation, have carcinogenic properties, and may result in respiratory and kidney issues. These chemicals are regarded as persistent, as they are not easily digested by microorganisms (Foroutan et al., 2022) (Blanco-Flores et al., 2014). Therefore, it is crucial to remove these dye pollutants from waterbodies.

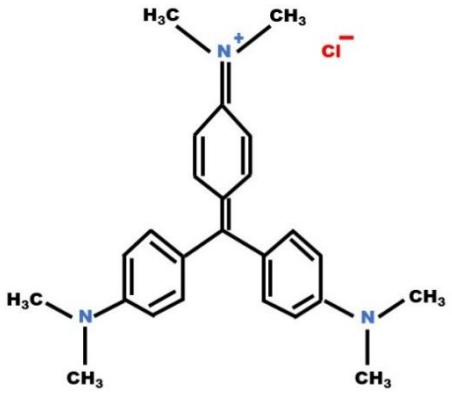

Fig. 1. Chemical structure of CV dye.

Recently, researchers have been growing interest in developing highly effective semiconducting photocatalysts to eliminate organic contaminants from wastewater through light irradiation and semiconducting materials. This offers an effective and cost-efficient method for cleaning wastewater (Asaithambi et al., 2019). There are multiple techniques for dye removal, including sedimentation, chemical precipitation, adsorption, advanced oxidation processes (AOPs), ultrafiltration, reverse osmosis, ion exchange, and heterogeneous photocatalysis (Adeleke et al., 2018; Shekhar Joshi et al., 2023). Recently, heterogeneous photocatalysis has become increasingly popular for dye removal due to its high efficiency and cost-effectiveness. Semiconducting metal oxides such as ZnO, TiO_2, SnO_2, Fe_2O_3, and WO_3 are often preferred materials for photocatalytic reactions (Ajeesha et al., 2021; Kim et al., 2016; Mohammed Harshulkhan et al., 2016; Slimani et al., 2023; Zhang et al., 2004). This preference is due to their excellent photostability, high photoactivity, biocompatibility, and the fact that they are relatively inexpensive and easy to produce. Among the different types of semiconducting metal oxides, tin oxide (SnO_2) nanostructures have garnered significant attention recently for their potential in photocatalytic applications. SnO_2 is an n-type semiconductor with a band gap energy of 3.6 eV, and it exhibits higher electron mobility compared to TiO_2 (Kar et al., 2019). Excellent transparency, high photosensitivity, chemical stability, affordability, and eco-friendliness are some of the other characteristics which makes SnO_2 an effective photocatalytic material (Ali Baig et al., 2020). However, SnO_2 faces limitations for large-scale applications due to its rapid recombination of photogenerated electron-hole pairs and low quantum yield in photocatalytic reactions, which affect its economic feasibility. Incorporating alkaline metals into the material alters the energy band

gap, which can improve its electronic properties and boost its photocatalytic performance. Doping SnO_2 with alkaline metals introduces lattice defects, such as oxygen vacancies, which enhances the generation of reactive oxygen species (ROS) (Asaithambi, Sakthivel, Karuppaiah, Hayakawa, et al., 2020). This process improves the photocatalytic efficiency of SnO_2 NPs. Appropriate metal doping can reduce the recombination of photogenerated electron-hole pairs during photocatalysis. Mg^{2+} (72 nm), with an ionic radius similar to that of Sn^{+4} (71 nm), is a promising option for doping in SnO_2 NPs (Kumari et al., 2014; Sabri et al., 2012; Xiong et al., 2016). Due to its non-toxic nature and cost-effectiveness, Mg^{2+} doping can enhance the photocatalytic properties of SnO_2 NPs. There are several chemical synthesis methods for producing SnO_2 NPs, including chemical precipitation, the sol-gel process (Aziz et al., 2013), microwave technique (Krishnakumar et al., 2009), chemical co-precipitation (Asaithambi, Sakthivel, Karuppaiah, Sankar, et al., 2020) and hydrothermal method (Patil et al., 2012). The chemical co-precipitation method is highly beneficial for synthesizing nanomaterials because it offers a simple and cost-effective way to consistently produce NPs with controlled sizes and specific shapes.

In this study, we extensively explore the photocatalytic activity of SnO_2 NPs that are doped with alkaline earth metal Mg. These NPs were synthesized using a straightforward co-precipitation method. The investigation covered the structural, optical and compositional characteristics of both undoped and alkaline metal-doped SnO_2 NPs. Additionally, the study includes a detailed analysis and discussion of the photocatalytic efficiency of these NPs.

2. MATERIALS AND METHODS

2.1. MATERIALS USED

Tin (IV) Chloride Pentahydrate ($SnCl_4.5H_2O$), Magnesium Nitrate Hexahydrate ($Mg(NO_3)_2{\cdot}6H_2O$), Sodium Hydroxide (NaOH) pellets, and Polyethylene Glycol (PEG), were used as reagent in this experiment. All these chemicals of Analytical Reagent (AR) grade were purchased from Hi-media and used directly without any further purification. Double distilled water was used for all experimental procedures.

2.2. SYNTHESIS OF MG-DOPED SNO_2 NPs

Homogeneous solutions of stannic chloride pentahydrate and appropriate amount (5 wt%, 10 wt% and 15 wt%) of magnesium nitrate hexahydrate ($Mg(NO_3)_2 \cdot 6H_2O$) in 50 ml of DI water were prepared separately. After 15 minutes of stirring, the solution containing magnesium nitrate hexahydrate was mixed with the tin (II) chloride pentahydrate and subsequently, 5 ml PEG was added to the resulting mixture. The mixture was further stirred for another 30 min and thereafter, 0.5M NaOH solution was added dropwise until the pH reached upto 12. The resulting mixture was then stirred for an additional 2 hours at 60°C. After completion of reaction, a thick off-white precipitate was formed at the bottom of the flask. The precipitate was collected and thoroughly rinsed with deionized water and ethanol to eliminate any impurities. The precipitate was dried at 60°C in a hot air oven for 10 hours. After drying, it was collected and ground using a mortar and pestle. The resulting powder was then placed in a crucible and calcinated at 450°C for 2 hours in a muffle furnace. After calcination tin oxide NPs were obtained. Pure and Mg-doped SnO_2 NPs are named as SM0, SM5, SM10 and SM15, where 0, 5, 10, and 15 represent the weight percentage of Mg in Mg-doped SnO_2 NPs.

2.3. CHARACTERIZATION TECHNIQUES

The purity, crystalline phase, and structure of synthesized NPs were analyzed using X-ray diffraction (XRD) with a Bruker D8-Advance diffractometer equipped with Cu Kα radiation (λ = 0.15418 nm. Fourier transform infrared (FTIR) spectra were recorded on an Alpha 200855 FTIR system. Optical properties were studied using UV-Vis spectrophotometer (LAMBDA 365, PerkinElmer) to measure absorbance.

2.4. PHOTOCATALYTIC DEGRADATION EXPERIMENT

The photocatalytic performance of the synthesized pure and Mg-doped SnO_2 NPs was evaluated by analyzing the degradation of crystal violet (CV) dye at a concentration of 10 mg/L under solar irradiation. The photocatalytic degradation of all the samples was examined by dispersing 20 mg catalyst in 100 ml dye solution. Before exposing the CV/photocatalyst solution to sunlight, the solutions were magnetically stirred for 1 hour at room temperature to attain adsorption-desorption equilibrium. After confirming the adsorption-desorption equilibrium, the photocatalysis was initiated by irradiating the CV/photocatalyst solution to sunlight. The dye degradation was tracked by periodically taking 2 ml samples from the

suspension and measuring their absorbance. The absorption spectra were recorded using UV–VIS spectrometer after centrifugation was performed to eliminate the suspended catalyst particles from the suspension. A UV–Visible spectrophotometer was employed to monitor how the concentration of CV dye changed over time. The CV solution were placed back into the beaker to maintain a consistent volume of the dye solutions after measuring the absorbance at each time point. The kinetics of CV photodegradation was studied using a pseudo-first-order kinetic equation (1) derived from the Langmuir-Hinshelwood model (Khairy & Zakaria, 2014):

$$ln(C_o/C_t) = kT \quad (1)$$

where C_O is the initial concentration of the dye (0 min), and C_t is the concentration of dye at time t. The rate constant, k, or equilibrium constant, is determined by analyzing the slope of the graph that plots $ln(C_o/C_t)$ against reaction time (t), according to relation (2) (Daniel Abraham et al., 2016):

$$k = 2.303 \times slope \quad (2)$$

The percentage efficiency (R %) of a photocatalyst (Senthil Kumar et al., 2015), was determined utilizing Equation (3):

$$\text{Degradation efficiency \%} = \left(\frac{C_O - C_t}{C_o}\right) \times 100 \quad (3)$$

This formula expresses the efficiency as a percentage by comparing the reduction in contaminant concentration to the initial amount.

3. RESULTS AND DISCUSSION

3.1. STRUCTURAL ANALYSIS

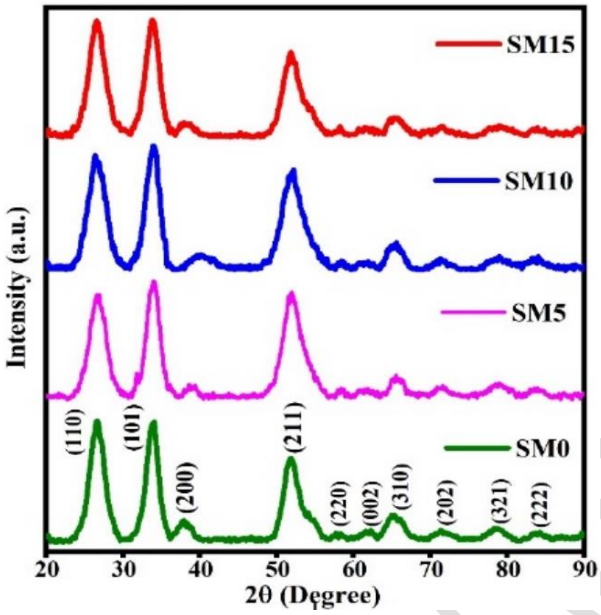

Fig 2. X-ray diffraction of pure SnO_2 and SnO_2: Mg NPs.

Fig.2 shows the XRD patterns of pure and Mg (5, 10 and 15 wt.%) doped SnO_2 NPs. All the samples are indexed with the tetragonal rutile phase of SnO_2. The diffraction peaks observed correspond to the (110), (101), (200), (211), (220), (002), (310), (202), (321), and (222) crystalline planes of the cassiterite phase of tetragonal SnO_2 at 2θ values of 26.69, 33.87, 38.01, 51.97, 57.93, 61.76, 65.38, 71.67, 78.61 and 84.01, respectively. These planes are align with the standard JCPDS card number 41-1445 (Kim et al., 2016). The average crystallite sizes (D) of the synthesized samples were determined using the Scherrer equation equation (4):

$$D = \frac{k\prime\lambda}{\beta Cos\theta} \qquad (4)$$

The constant k' is Scherrer constant or particle shape factor k having value 0.9, while λ represents the X-ray wavelength, which is 0.154 nm. The variables β and θ are full width at half maximum (FWHM) and diffraction angle, respectively. The absence of Mg peak in the XRD pattern could be attributed to the effective dispersion of Mg within the SnO_2 NPs, as well as the low concentration of Mg. The average crystallite size, exhibited a slight variation when Mg was doped under the same experimental conditions.

Microstrain (ε), lattice parameters 'a=b' and 'c' and lattice strain (δ) was determined using the following equations (5-7) (Madiba et al., 2017; Mirzayev et al., n.d.; Sudha et al., 2016):

$$\varepsilon = \frac{\beta}{4\tan\theta} \quad (5)$$

$$\frac{1}{d^2} = \frac{h^2+k^2}{a^2} + \frac{l^2}{c^2} \quad (6)$$

$$\delta = \frac{1}{D^2} \quad (7)$$

Where h, k, and l represent the Miller indices, a=b and c are the lattice parameters, and d denotes the interplanar spacing.

Table 1. The structural parameters of Un-doped and Mg-doped SnO_2 NPs.

Sample	(hkl)	2θ(°)	β ($\times10^{-3}$) rad	Average crystallite size D (nm)	δ ($\times10^{-2}$lines nm^{-2})	ε ($\times10^{-3}$)	Lattice constants (Å)	
							a	c
SM0	110	26.69	0.0332	4.49	5.437	0.0350	4.7404	3.1929
	101	33.87	0.0266		3.388	0.0219		
SM5	110	26.75	0.0375	4.39	6.951	0.0395	4.7369	3.1859
	101	33.95	0.0292		4.081	0.0239		
SM10	110	26.65	0.0406	3.80	8.147	0.0429	4.7212	3.1962
	101	33.91	0.0304		4.413	0.0249		
SM15	110	26.66	0.0361	3.72	6.421	0.0380	4.6885	3.1797
	101	33.87	0.0304		4.422	0.0250		

3.2. FOURIER TRANSFORM INFRARED (FTIR) ANALYSIS

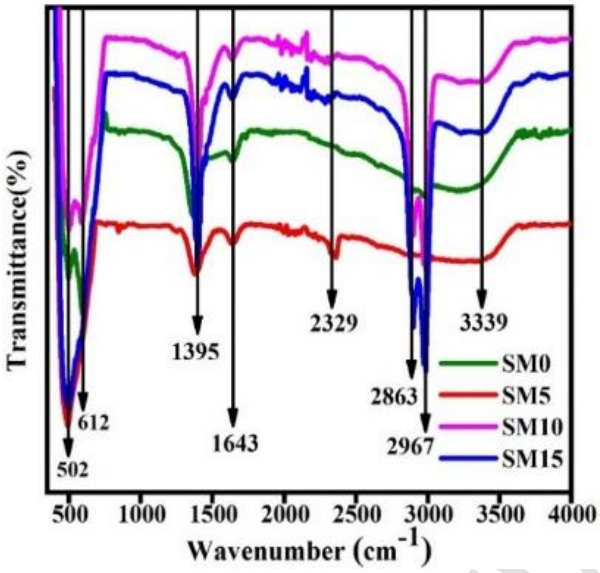

Fig 3. FTIR spectra of Mg-doped SnO_2 NPs.

Fig. 3 presents the FTIR spectra for both pristine and Mg-doped SnO_2 NPs, recorded over the wavenumber range of 400 to 4000 cm^{-1} after the sample powder was diluted with KBr. The broad and intense band in the range of 3000–3600 cm^{-1} are the characteristic of stretching vibrational modes of O–H bond, which are attributed to the Sn-OH groups and adsorbed water molecules (Farrukh et al., n.d.; Pascariu et al., 2016). The peaks observed around 1643 cm^{-1} correspond to the O-H bending vibrations are associated with residual water molecules used during mixing of KBr binder for measurement (Nachiar & Muthukumaran, 2019). The feeble band observed at 2329 cm^{-1} might be attributed to the absorption of CO_2 from ambient air atmosphere (Jouhannaud et al., 2008). The symmetric and asymmetric C–H vibrations were observed at 2967 cm^{-1} and 2863 cm^{-1}, respectively. This implies that the NPs are essentially capped with the ethylene glycol used in their synthesis (Nachiar & Muthukumaran, 2019; Singh et al., 2014). The prominent absorption bands observed in the lower-wavenumber region (400–800 cm^{-1}), particularly at 502 and 612 cm^{-1}, are characteristic IR fingerprints of the doped SnO_2 NPs. These bands correspond to anti-symmetric O–Sn–O vibrations and the Sn–O (terminal oxygen vibration of Sn–OH) lattice-extending vibrations, respectively (Dobrucka et al., 2018; Manjula & Selvan, 2017). Furthermore, the bands detected around 1379 cm^{-1} are ascribed to the bending vibrations of the C=O bond (Zhou et al., 2018).

However, no specific peaks corresponding to Mg–O bonds were observed, indicating the incorporation of Mg into the SnO_2-structured matrix as observed in the XRD analysis. A minor variation is noticed in the intensity and position of these characteristic bands. This effect is due to the larger ionic radii of alkaline metal ions Mg^{2+} compared to Sn^{4+}, which alters the SnO_2 lattice. Additionally, these dopant ions may occupy interstitial sites, contributing to shift in the IR absorption spectrum (Asaithambi, Sakthivel, Karuppaiah, Hayakawa, et al., 2020). Absorption band position along with corresponding assigned functional groups in samples are given. in Table 2.

Table 2. Absorption band position along with corresponding assigned functional groups in samples.

Absorption bands (~ cm^{-1})	Functional group	Reference
473	Sn-O stretching mode of vibration	(Dobrucka et al., 2018; Manjula & Selvan, 2017)
607	O-Sn-O stretching mode of vibration	(Dobrucka et al., 2018; Manjula & Selvan, 2017)
1379	C=O bond stretching vibration	(Zhou et al., 2018)
1637	Bending vibration of surface hydroxyl (-OH) groups	(S. Kumar et al., 2015)
2863	Asymmetric vibration attributed to C-H bonds	(Singh et al., 2014)
2967	Symmetric vibration attributed to C-H bonds	(Nachiar & Muthukumaran, 2019; Singh et al., 2014)
3332	Stretching vibration of surface hydroxyl (-OH) groups	(S. Kumar et al., 2015)

3.3. OPTICAL STUDIES

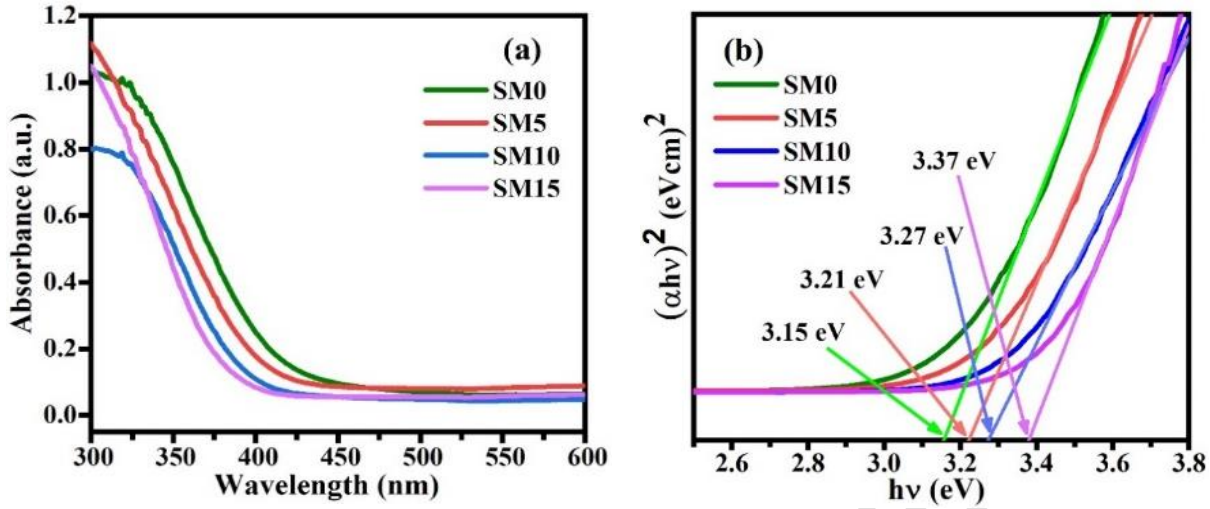

Fig. 4. (a) UV-visible absorption spectra and (b) Tauc's plot of un-irradiated and γ-irradiated Mg-doped SnO_2 NPs.

Fig. 4 (a) represents the optical absorption spectra for pure and Mg-doped SnO_2 NPs recorded in the range of 300 to 800 nm. Absorbance is expected to be influenced by various factors, including band gap, oxygen deficiency, surface roughness, and impurity centers (A. S. Ahmed et al., 2011). The absorption edge of various samples varies with the concentration of Mg in SnO_2 NPs. As the Mg content increases in the SnO_2 host, a noticeable shift towards lower wavelengths (blue shift) is observed in the absorption edge which may lead to an increment in band gap.

The optical bandgap of pure and Mg-doped SnO_2 NPs were determined using Tauc plots method equation (8):

$$(\alpha h\nu) = B(h\upsilon - E_g)^n \quad (8)$$

Here, α represents the absorption coefficient, A is a constant, v denotes frequency, h stands for Planck's constant, and Eg represents the bandgap energy. The parameter n equals ½ specifically for the direct bandgap of the semiconductor.

The optical band gap (E_g) can be determined by extrapolating linear region of a plot of $(\alpha h\nu)^2$ vs hv. Fig. 4(b) graphically represents the plot of $(\alpha h\nu)^2$ versus hv for the synthesized SnO_2 NPs. The measured

band gap values for Mg-doped SnO_2 with doping concentrations of 0%, 5%, 10%, and 15% are 3.15 eV, 3.21 eV, 3.27 eV, and 3.37 eV, respectively. The results showed that doping Mg led to an increase in the band gap energy of pure SnO_2 resulting in a blue shift. The rise in the band-gap suggested that Mg was effectively integrated into the SnO_2 crystal structure. The observed rise in Eg could be attributed to the quantum confinement effect (Mohana Priya et al., 2016). Moreover, observed increase in the band gap with an increase in Mg doping can be attributed to the dominance of d-d transitions over sp-d transitions (Nyamukamba et al., 2017).

3.4. PHOTOCATALYTIC DEGRADATION STUDIES:

The synthesized pure and Mg-doped SnO_2 NPs were employed as photocatalysts for the degradation of CV dye under solar irradiation. The absorption of CV dye was measured using UV–Visible spectrophotometer. The UV–Visible spectra for the CV dye solutions degraded by synthesized samples as a photocatalyst are displayed in Fig. 5.

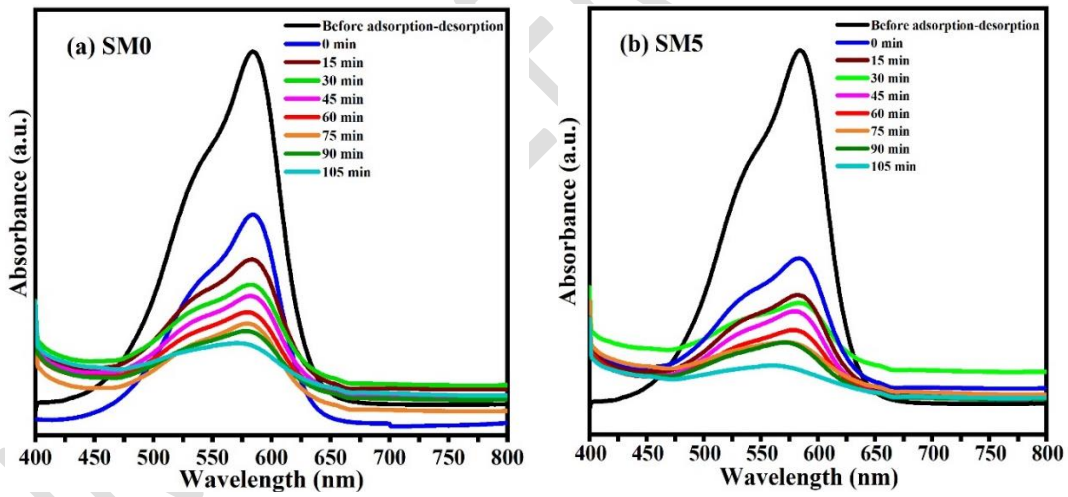

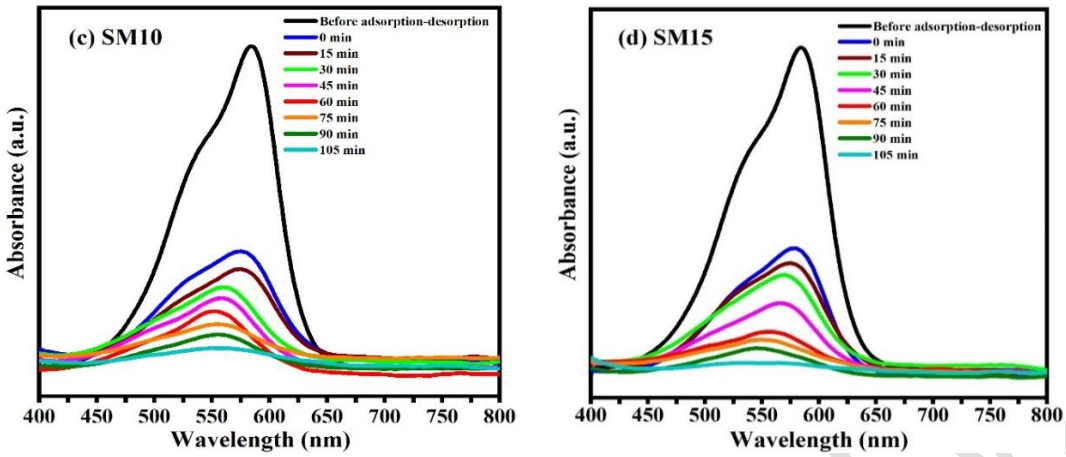

Fig.5. UV-Vis absorption spectra of CV dye for (a) SM0, (b) SM5, (c) SM10, and (d) SM15.

The change in dye concentration with time of reaction for pure and Mg-doped SnO_2 NPs is depicted in Fig. 6 (a). From Fig. 6(a), it can be observed that highest effectiveness is achieved by the SM15 photocatalyst. The dye degradation process follows pseudo-first-order kinetics. The graph for pseudo-first-order kinetics is plotted with $\ln(C_O/C_t)$ against the reaction time for each of the synthesized photocatalysts. Fig. 6 (b) represents the pseudo-first-order kinetic plots for all the samples. The linearity observed in the plots for all the samples suggested that pseudo-first-order kinetics are applicable. The enhanced photocatalytic performance is attributed to a larger surface area, the availability of more reactive ions, and an increase in active sites.

The rate constant for the degradation reactions of the synthesized photocatalysts were determined using equation (2). The rate constants calculated for the degradation of CV dye are plotted against the synthesized photocatalyst, as illustrated in Fig. 7 (a). The calculated values of rate constants are 0.02073, 0.02464, 0.03385 and 0.0552 for SM0, SM5, SM10 and SM15, respectively. Table 3. shows the linear regression coefficient (R^2), reaction rate constant (k), and percentage of degradation efficiency for each sample for the degradation process of CV dye.

Table 3. Band gap, Rate constant (k) and linear regression coefficient R^2 values of the photocatalyst.

Samples	Band gap E_g (eV)	Irradiation time (min)	Degradation efficiency (%)	Rate constant K (min^{-1})	R^2
SM0	3.15	105	67	0.02073	0.97
SM5	3.21	105	72	0.02464	0.95
SM10	3.27	105	81	0.03385	0.96
SM15	3.37	105	93	0.05527	0.91

The degradation of the CV dye under solar light exposure, using 10 mg of the prepared photocatalysts, is illustrated in Figure 7(b) by plotting the efficiency of degradation as a function of reaction time. SM15 photocatalyst shows maximum degradation efficiency of 93% over time of 105 min whereas SM0 photocatalyst possesses degradation efficiency of merely 67%. The low efficiency of pure SnO_2 can be attributed to the rapid recombination of charge carriers. This rapid recombination reduces the probability of the movement of the photo-generated charge carriers reaching the catalyst surface, which in turn diminishes photocatalytic activity (Maleki et al., 2015). (V. B. Kumar et al., 2017).

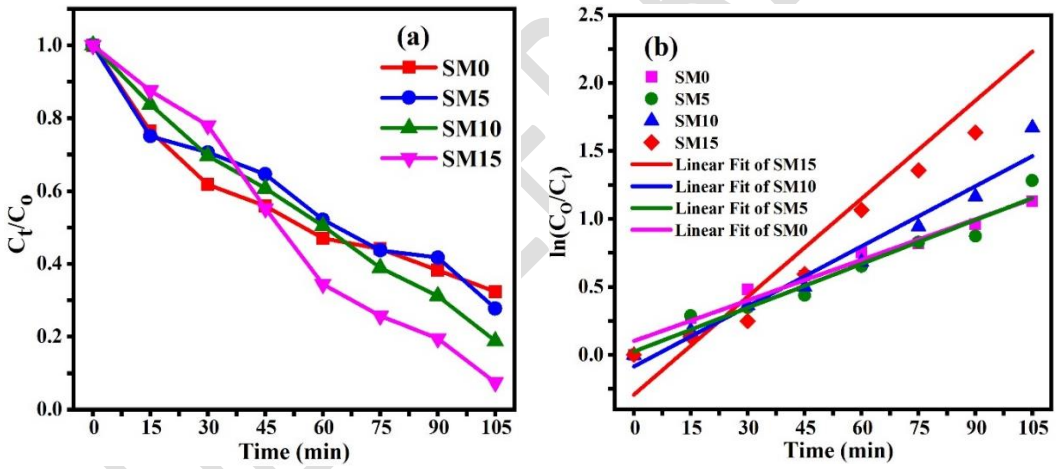

Fig. 6. (a) Relative concentration vs time plot of CV dye (b) Pseudo first-order kinetics for the degradation of CV dye for different catalysts.

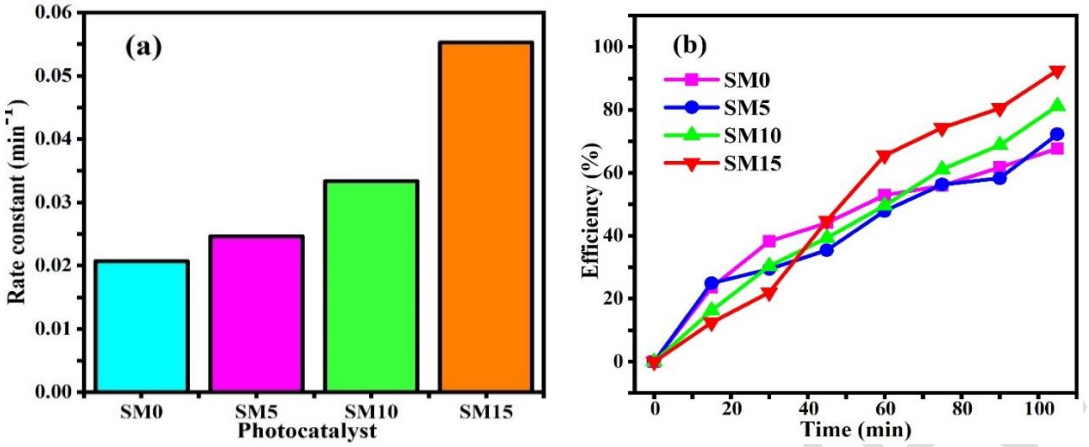

Fig. 7. (a) Representation of rate constant through Histogram (b) Time-dependent degradation efficiency of the samples.

The findings indicated that 15 wt% Mg-doped SnO_2 photocatalysts exhibit outstanding photocatalytic performance in breaking down CV dye. The enhancement in photocatalytic performance resulting from Mg doping can be linked to a blue shift, which is explained by the Burstein–Moss effect (Karthikeyan & Pandiyarajan, 2010). The Fermi level in Mg-doped SnO_2 NPs may be positioned at a higher energy level, causing a shift in the absorption edge towards shorter wavelengths. A larger band gap energy is associated with a higher redox potential of electron-hole pairs, which in turn leads to enhanced photocatalytic activity. Similar results are reported by (Behnajady & Tohidi, 2014). Also based on the XRD results of this study, the reduction in crystallite size leads to an increased surface-to-volume ratio, which significantly improves the photocatalytic capabilities (Bindu & Thomas, 2014). It is important to note that a material with lower band gap doesn't necessarily exhibit higher photocatalytic activity as might be expected. The photocatalytic performance of SM0 photocatalyst with calculated band gap of 3.15 eV was surprisingly lower than that of SM15 photocatalyst, which had band gap of 3.37 eV, despite expectations based on their band gap values. This observation indicated that narrowing the band gap can enhance the absorption of light, although it does not necessarily lead to improved photocatalytic activity under visible light conditions. This suggested that factors beyond band gap narrowing may influence the photocatalytic activity of SnO_2 NPs. These factors may include rate of electron-hole recombination, hydrophilicity, and variations in surface

area and surface properties that can enhance adsorption. Table 4. presents a comparative analysis of our study alongside other recent research on the degradation of CV dye using various photocatalysts.

Table 4. Comparison of photocatalytic activity of present work with other nanomaterials for the degradation of different organic dyes.

Photocatalyst	Dose (mg)	Dye	Dye concentration (mg/	Light source	Degradation time (min)	Degradation Efficiency (%)	References
Mg-doped CuFeO2	50	Methylene Blue (MB)	50 ppm (50 ml)	Visible light source.	90	92.7	(Chang et al., 2021)
ZnO	150	Crystal Violet (CV)	10 (100 ml)	UV irradiation	120	90	(Franco et al., 2019)
Gd doped BFO	200	Crystal Violet (CV)	20	Mercury lamp 250 W	105	84.5	(Kossar et al., 2021)
Mg-doped ZnO	200	Methylene blue (MB)	10^{-5} M (200 mL)	Xenon lamp	60	99	(Sa-nguanprang et al., 2019)
Titanate nanosheets (TNT	20	Crystal Violet (CV)	200 (20ml)	UV lamp 16 W	75	100	(Rashad et al., 2019)
Mg-doped TiO_2	100	Methylene orange (MO)	10 (100 ml)	UV light	120	47.82	(Athira et al., 2020)
N doped SnO_2	100	Crystal Violet (CV)	20×10^{-6} M (100 ml)	UV Light irradiation	90	73	(Bhawna et al., 2023)
Glutamine-assisted SnO_2 nanorods	10	Crystal Violet (CV)	20 (100 ml)	Mercury lamp 250W	60	97.3	(Alharbi et al., 2022)
Mg-doped CuFeO2	50	Methylene Blue (MB)	50 ppm (50 ml)	Visible light source.	90	92.7	(Chang et al., 2021)
$SrFe_2O_4$	50	Crystal Violet (CV)	10 (50 ml)	Microwave irradiation	10	88.6	(Liu et al., 2018)
Mg-doped ZnO	50	Rhodamine B (RhB)	20 ppm (150 ml)	UV 125 W	120	78	(Pradeev raj et al., 2018)
$BaFe_2O_4$	50	Crystal Violet	10 (50 ml)	Microwave irradiation	10	96.6	(Liu et al., 2016)
Mg-doped CuO	200	Methylene Blue (MB)	20 μM (300 mL)	UV Hg lamp 450 W	180	95.71	(Azharudeen et al., 2022)
Sn@C-dots/TiO2 t	60	Crystal Violet (CV)	_(100 ml)	Sunlight	210	60	(V. B. Kumar et al., 2017)

Mg-doped CeO_2	10	Methylene Blue (MB) dye	20 ppm (200 ml)	UV (20 W)	120	75.2	(Murugan et al., 2018)
MoS_2 NFs	20	Crystal Violet (CV)	0.1 (100 ml)	Sunlight	40	99.3	(Sadhanala et al., 2018)
SM0	20	Crystal Violet (CV)	10 (100 ml)	Sunlight	105	67	This work
SM5	20	Crystal Violet (CV)	10 (100 ml)	Sunlight	105	72	This work
SM10	20	Crystal Violet (CV)	10 (100 ml)	Sunlight	105	81	This work
SM15	20	Crystal Violet (CV)	10 (100 ml)	Sunlight	105	93	This work

3.5. PHOTOCATALYTIC DEGRADATION MECHANISM

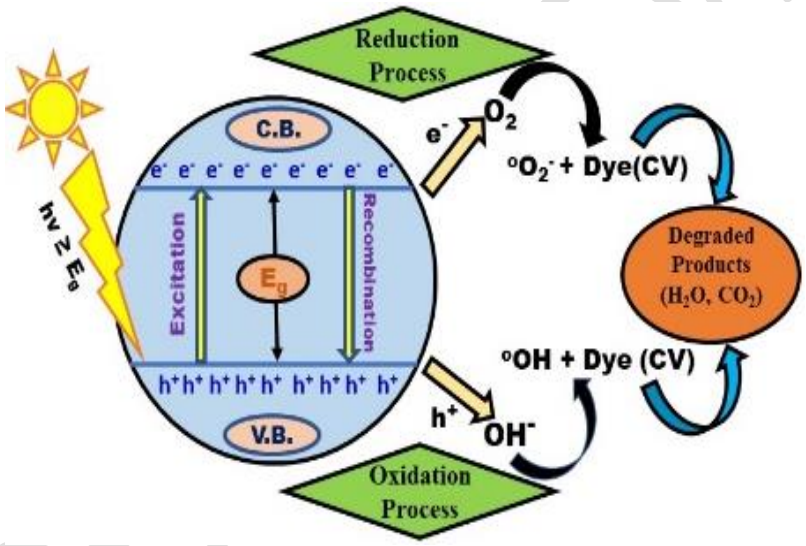

Fig. 8. Mechanism of Mg-doped SnO_2 NPs Facilitated Photocatalytic Breakdown of Crystal Violet (CV) Dye.

Fig 8. illustrates the process of photocatalytic degradation of CV dye employing Mg-doped SnO_2 photocatalyst. When exposed to sunlight, SnO_2 can absorb photons causing an electron to move from the valence band to the conduction band (V. B. Kumar et al., 2017). Generally, these electron-hole pairs tend to recombine rapidly, leaving insufficient time for them to engage in any catalytic reaction (Sharma et al., 2019). The recombination of electron-hole pairs can be reduced, by incorporating Mg into SnO_2 NPs. Hence, electrons and holes move more efficiently to the surface of catalyst, where they engage in redox

reactions with adsorbed species. The isolated holes in the valence band (VB) of SnO_2 can interact with water molecules to produce hydroxyl radicals. At the same time, the electrons that are captured by Mg ions are transferred to oxygen molecules, leading to the formation of reactive superoxide radicals (Sadhanala et al., 2018). These superoxide radicals are then converted into hydroxyl radicals through multiple electron reduction steps, as described in Equations (9-14). The reactive radicals produced may partially or entirely oxidize organic pollutants, transforming them into harmless substances or degraded products i.e., CO_2 and H_2O. This proposed mechanism is depicted in Fig. 8, which illustrates the potential degradation process of organic pollutants under sunlight exposure. The reaction mechanism for the photocatalytic degradation of CV dye in the presence of sunlight can be described as follows (A. Ahmed et al., 2019):

$$\mathrm{Mg-SnO_2} + h\nu \longrightarrow Mg - SnO_2 + e^-_{(CB)} + h^+_{(VB)} \quad (9)$$

$$Mg - \mathrm{SnO_2} + e^-_{(CB)} + O_2 \longrightarrow {}^{o}O_2^- \quad (10)$$

$${}^{o}O_2^- + e^- + 2H^+ \rightarrow H_2O_2 \quad (11)$$

$$H_2O_2 + e^- \longrightarrow {}^{\circ}OH + OH^- \quad (12)$$

$$\mathrm{Mg-SnO_2} + h^+_{(VB)} + H_2O \longrightarrow H^+ + {}^{\circ}OH \quad (13)$$

$$\text{Organic pollutant} + {}^{\circ}OH \longrightarrow degraded\ products \quad (14)$$

4. CONCLUSION

Pure and Mg-doped SnO_2 nanoparticles were synthesized using the chemical co-precipitation method. The XRD analysis reveals that the nanoparticles possess an average size of 4-3 nm and exhibit tetragonal rutile phase of SnO_2. The FTIR spectra validated the synthesis of Mg-doped SnO_2 nanoparticles, indicating the presence of both Sn-O-Sn and Sn-O bands. The band gap of the samples was explored using UV-visible absorption spectroscopy, revealing an increment in band gap from 3.15 eV for undoped (SM0) to 3.37 eV for 15 wt% (SM15) Mg-doped SnO_2 NPs. Among the tested samples, 15 wt% SnO_2 sample exhibited the most effective photocatalytic activity. The study revealed that a photocatalyst with a lower band gap does not necessarily exhibit superior photocatalytic activity compared to wide band gap photocatalysts under visible light irradiation, contrary to what might be anticipated. Other factors like surface

area, electron-hole recombination and hydrophilicity can surpass band gap narrowing in boosting the overall efficiency of the photocatalyst. This research could offer novel perspectives on the development of semiconducting metal oxide nanoparticles with potential applications in photocatalysis.

References

Al-Tohamy R, Ali SS, Li F, Okasha KM, Mahmoud YA, Elsamahy T, Jiao H, Fu Y, Sun J. A critical review on the treatment of dye-containing wastewater: Ecotoxicological and health concerns of textile dyes and possible remediation approaches for environmental safety. Ecotoxicology and Environmental Safety. 2022 Feb 1;231:113160.

Foroutan M, Bavani BM, Boudaghi A. Controlled hydrophilization of black phosphorene: a reactive molecular dynamics simulation approach. Physical Chemistry Chemical Physics. 2022;24(44):27532-47.

Blanco-Flores AL, Colín-Cruz AR, Gutiérrez-Segura E, Sánchez-Mendieta V, Solís-Casados DA, Garrudo-Guirado MA, Batista-González R. Efficient removal of crystal violet dye from aqueous solutions by vitreous tuff mineral. Environmental technology. 2014 Jun 18;35(12):1508-19.

Asaithambi S, Murugan R, Sakthivel P, Karuppaiah M, Rajendran S, Ravi G. Influence of Ni doping in SnO2 nanoparticles with enhanced visible light photocatalytic activity for degradation of methylene blue dye. Journal of nanoscience and nanotechnology. 2019 Aug 1;19(8):4438-46.

Adeleke AQ, Bahaudin AY, Kamaruddeen AM, Bamgbade JA, Salimon MG, Khan MW, Sorooshian S. The influence of organizational external factors on construction risk

management among Nigerian construction companies. Safety and health at work. 2018 Mar 1;9(1):115-24.

Joshi CS, Srivastava RC, Joshi A. Polyaniline/Manganese-Cobalt ferrite nanocomposite as an efficient material for crystal violet dye degradation under sunlight irradiation. Materials Today: Proceedings. 2023 May 6.

Ajeesha T, Ashwini A, George M, Manikandan A, Mary JA, Slimani Y, Almessiere MA, Baykal AJ. Nickel substituted MgFe2O4 nanoparticles via co-precipitation method for photocatalytic applications. Physica B: Condensed Matter. 2021 Apr 1;606:412660.

Mohammed Harshulkhan S, Janaki K, Velraj G, Sakthi Ganapthy R, Nagarajan M. Effect of Ag doping on structural, optical and photocatalytic activity of tungsten oxide (WO3) nanoparticles. Journal of Materials Science: Materials in Electronics. 2016 May;27(5):4744-51.

Baig AM, Khaleeq A, Ali U, Syeda H. Evidence of the COVID-19 virus targeting the CNS: tissue distribution, host–virus interaction, and proposed neurotropic mechanisms. ACS chemical neuroscience. 2020 Mar 13;11(7):995-8.

Asaithambi S, Sakthivel P, Karuppaiah M, Hayakawa Y, Loganathan A, Ravi G. Improved photocatalytic performance of nanostructured SnO 2 via addition of alkaline earth metals (Ba 2+, Ca 2+ and Mg 2+) under visible light irradiation. Applied Physics A. 2020 Apr;126:1-2.

Krishnakumar T, Jayaprakash R, Pinna N, Donato N, Bonavita A, Micali G, Neri G. CO gas sensing of ZnO nanostructures synthesized by an assisted microwave wet chemical route. Sensors and Actuators B: Chemical. 2009 Dec 4;143(1):198-204.